This is a preprint, the final version is subject to change, of the American Mineralogist (MSA)
Cite as Authors (Year) Title. American Mineralogist, in press.
DOI: https://doi.org/10.2138/am-2019-6740

Revision 1

High-pressure phase transitions of clinoenstatite

John D. Lazarz[1,*], Przemyslaw Dera[2], Yi Hu[2,3], Yue Meng[4], Craig R. Bina[1], and Steven D. Jacobsen[1]

[1]Department of Earth and Planetary Sciences, Northwestern University, Evanston, IL 60208, USA

[2]Hawaii Institute of Geophysics and Planetology, School of Ocean and Earth Science and Technology, University of Hawai'i at Manoa, Honolulu, HI 96822, USA

[3]Department of Geology and Geophysics, School of Ocean and Earth Science and Technology, University of Hawai'i at Manoa, Honolulu, HI 96822, USA

[4]HPCAT, Advanced Photon Source, Argonne National Laboratory, Argonne, IL 60439, USA

*Present address: Shock and Detonation Physics, Los Alamos National Laboratory, Los Alamos, NM 87545, USA

Abstract

Clinoenstatite ($Mg_2Si_2O_6$) undergoes a well-known phase transition from a low-pressure form (LPCEN, space group $P2_1/c$) to a high-pressure form (HPCEN, space group $C2/c$) at ~6 GPa. High-pressure structure refinements of HPCEN were carried out based on single-crystal X-ray diffraction experiments between 9.5 and 35.5 GPa to determine its *P-V* equation of state and structural evolution over an expanded pressure range relevant to pyroxene metatstability. A third-order Birch Murnaghan equation of state was fitted to the compression data resulting in V_0 = 406(1) Å^3, K_{T0} = 103(8) GPa, and K_0' = 5.4(0.6). At ~45 GPa, a transition from HPCEN to a $P2_1/c$-structured polymorph (HPCEN2) was observed, which is clearly related to the $P2_1/c$ structure recently observed in diopside ($CaMgSi_2O_6$) at 50 GPa (Plonka et al. 2012) and in clinoferrosilite ($Fe_2Si_2O_6$) at ~30-36 GPa (Pakhomova et al. 2017). Observation of HPCEN2 in

This is a preprint, the final version is subject to change, of the American Mineralogist (MSA)
Cite as Authors (Year) Title. American Mineralogist, in press.
DOI: https://doi.org/10.2138/am-2019-6740

$Mg_2Si_2O_6$ completes the third apex of the pyroxene quadrilateral wherein HPCEN2 is found, facilitating a broader view of clinopyroxene crystal chemistry at conditions relevant to metastability in the Earth's mantle along cold subduction geotherms.

Keywords

$MgSiO_3$, clinoenstatite, enstatite, pyroxene, single-crystal X-ray diffraction

This is a preprint, the final version is subject to change, of the American Mineralogist (MSA)
Cite as Authors (Year) Title. American Mineralogist, in press.
DOI: https://doi.org/10.2138/am-2019-6740

Revision 1

Introduction

Pyroxenes are a major component of the Earth's crust and upper mantle, constituting around 25% by volume of the pyrolite model from 100-400 km depth (Ringwood 1977; Akaogi and Akimoto 1977). The components of both orthopyroxene $(Mg,Fe)SiO_3$ and clinopyroxene-$CaMgSi_2O_6$ are incorporated into pyrope and majoritic garnet at depths from 300-500 km, however under the colder conditions along subducting slabs it is possible for metastable pyroxenes to persist deep in the upper mantle (e.g. Hogrefe et al. 1994; Nishi et al. 2013; Van Mierlow et al. 2013; King et al. 2015; Agrusta et al. 2014; Finkelstein et al. 2014; Bina 2013). Pyroxenes penetrating the mantle to such depths could potentially undergo further phase transitions impacting subducting slab mineralogy and mantle dynamics.

The major pyroxenes relevant to mafic-ultramafic rocks and the Earth's upper mantle are characterized by single chains of corner-sharing SiO_4 tetrahedra interconnected by MO_6 octahedra containing M cations Mg, Fe, or Ca forming the pyroxene compositional quadrilateral with end members enstatite (En, $Mg_2Si_2O_6$), ferrosilite (Fs, $Fe_2Si_2O_6$), diopside (Di, $MgCaSi_2O_6$), and hedenbergite (Hd, $CaFeSi_2O_6$) (Morimoto et al. 1989). Low-Ca pyroxenes along the En-Fs join are orthorhombic (Pbca), and hence known as orthopyroxenes, whereas Ca-bearing pyroxenes in the quadrilateral are monoclinic and hence called clinopyroxenes (cpx). Ca-rich cpx crystallize in $C2/c$ while Ca-poor cpx crystalize in $P2_1/c$.

Orthoenstatite-$Mg_2Si_2O_6$ (OEN) is a major phase of peridotite and was found to transform to a monoclinic, high-pressure clinoenstatite (HPCEN) with space group $C2/c$ along a phase boundary corresponding to ~200-250 km depth (e.g. Pacalo and Gasparik 1990; Angel et al. 1992), suggesting that the transformation might be associated with upper-mantle seismic discontinuities, namely the Lehman discontinuity or the X-discontinuity (e.g. Angel et al. 1992;

This is a preprint, the final version is subject to change, of the American Mineralogist (MSA)
Cite as Authors (Year) Title. American Mineralogist, in press.
DOI: https://doi.org/10.2138/am-2019-6740

Kung et al. 2004; Ferot et al. 2012; Deuss and Woodhouse 2004; Revenaugh and Jordan 1991). In experiments, the HPCEN phase quenches to the monoclinic, low-pressure clinoenstatite (LPCEN) with space group $P2_1/c$, which is however rare in nature (e.g. Poldervaart and Hess 1951; Shiraki et al. 1980).

On compression, transformation from LPCEN to HPCEN at 300 K varies from 6 to 8 GPa, depending on Fe-content, water content, and stress (e.g. Ross and Reynard 1999; Jacobsen et al. 2010). With both OEN and LPCEN transforming to HPCEN at pressures below 10 GPa, it has been presumed that HPCEN is the stable phase of $(Mg,Fe)_2Si_2O_6$ below ~250 km depth. The reference physical properties of HPCEN are not well constrained because it is not a quenchable phase, however, in situ sound velocity measurements by Kung et al. (2004) were used to determine its adiabatic elastic moduli at a reference pressure of 6.5 GPa, with K_S = 156.7(8) GPa and G = 98.5(4) GPa. Previous volume-compression studies across the LPCEN-HPCEN transition estimated the zero-pressure isothermal bulk modulus of HPCEN to be $K_{T0} \approx 118$ GPa (Jacobsen et al. 2010) and K_{T0} = 104(6) GPa (Angel and Hugh-Jones 1994), but these studies relied on extrapolation from very few data points over a very limited pressure range of ~6-8 GPa.

We investigated the volume and structural compression behavior of HPCEN from single-crystal X-ray diffraction measurements at 10-35 GPa. At 45 GPa, we observed a new phase of $Mg_2Si_2O_6$ with space group $P2_1/c$. This phase, a second monoclinic high-pressure clinoenstatite (HPCEN2) is analogous to the high-pressure clinopyroxene found in clinoferrosilite-$Fe_2Si_2O_6$ at 30-36 GPa (Pakhomova et al. 2017) and in diopside-$CaMgSi_2O_6$ at ~50 GPa (Plonka et al. 2012; Hu et al. 2016), providing further evidence that the HPCEN2 structure is common to phases in the pyroxene quadrilateral. The pressure-temperature-compositional dependence of the HPCEN

This is a preprint, the final version is subject to change, of the American Mineralogist (MSA)
Cite as Authors (Year) Title. American Mineralogist, in press.
DOI: https://doi.org/10.2138/am-2019-6740

to HPCEN2 transition has implications for understanding potential pyroxene metastability along cold subduction geotherms and may impact models of slab dynamics.

Experimental Methods

High-pressure X-ray diffraction

Synthesis of LPCEN single crystals used in this study was described previously (Jacobsen et al. 2010). Briefly, powdered MgO and SiO_2 starting materials were mixed in 1:1 molar proportion and heated at 950 °C for six hours in a flux of V_2O_5, MoO_3, and Li_2CO_3 in molar proportions of 1:7:9. The run products consisted primarily of low-clinoenstatite, with minor amounts of orthoenstatite and quartz. LPCEN crystals were selected for diffraction experiments using Raman spectroscopy to confirm the presence of the 369 and 431 cm^{-1} vibrational bands, the distinguishing feature from orthoenstatite (Ulmer and Stalder 2001).

High-pressure, single-crystal X-ray diffraction (XRD) experiments were carried out at HPCAT, Sector 16 experimental station 16ID-B of the Advanced Photon Source (APS), Argonne National Laboratory (ANL). Diamond anvil cell XRD measurements spanned the pressure range 9.5 to 50 GPa. A rhenium gasket with initial thickness of 250 μm was pre-indented to ~40 μm using 300 μm culet Bohler-Almax type diamond anvils. Two 30 μm diameter, approximately 20 μm thick, single crystals were loaded into the sample chamber along with two ruby spheres. Differential stresses within the sample chamber were minimized by loading neon as a pressure medium using the GSECARS/COMPRES gas loading system (Rivers et al. 2008). Pressure was determined using the ruby fluorescence method (Mao et al. 1986).

The diffraction experiments used a monochromatic X-ray beam with wavelength 0.351453 Å, focused with a Kirkpatrick-Baez mirror system to ~0.005 mm, full-width half maximum, in both horizontal and vertical directions. A MAR165 charge-coupled device (CCD)

This is a preprint, the final version is subject to change, of the American Mineralogist (MSA)
Cite as Authors (Year) Title. American Mineralogist, in press.
DOI: https://doi.org/10.2138/am-2019-6740

detector was placed roughly 170 mm away from the sample, and LaB_6 powder was used to calibrate the distance and tilt of the detector. The diffraction-accessible angular opening of the diamond cell was ± 33° during the data collection. On increasing pressure, a series of step and wide-step ω-scans were collected. Step scans involved 1° angular increments, while wide-step scans had 16.5° angular increments. The exposure time was at 1 second per degree. After collection of step and wide-step ω-exposures at the zero detector position, more wide-step ω-exposures were recorded with the detector translated horizontally, perpendicular to the X-ray beam by 70 mm. Exposure rates for the off-center detector positions were 2 seconds per degree. Step scans were used to obtain intensities for structural refinement.

Diffraction images were analyzed using GSE_ADA and RSV software packages (Dera 2007). Least-squares structure refinements were performed at every pressure point using SHELXL (Sheldrick 2008). In all refinements displacement parameters were treated as isotropic and site occupancy factors were fixed with the tetrahedral sites fully occupied by Si and the two octahedral sites occupied by Mg. Neutral scattering factors were used. Refinements statistics are listed in Table 1. Structure refinement results can be found in supplementary CIF files.

Density functional theory calculations

In order to obtain some thermodynamic interpretation of the three phases observed in the experiments, we performed a series of crystal structure optimizations and electronic structure calculations using density functional theory (DFT), as implemented in the Vienna Ab Initio Simulation Package (VASP) version 5.4 (Kresse and Hafner 1993), controlled by MedeA interface, version 2.22.1. All density functional calculations used the Perdew-Burke-Ernzerhof (PBE) generalized gradient approximation (GGA) (Perdew et al. 1996). The projector augmented wave (PAW) method (Blöchl 1994) was used to treat the core states with a plane wave basis set.

This is a preprint, the final version is subject to change, of the American Mineralogist (MSA)
Cite as Authors (Year) Title. American Mineralogist, in press.
DOI: https://doi.org/10.2138/am-2019-6740

The Si $3s^2/3p^2$, O $2s^2/2p^4$ and Mg $3s^2$ electrons were treated explicitly using the PAW-PBE Si, O and Mg POTCARs, which are available in MedeA. The energy cutoff was set to be 520 eV. The k-point grids were generated using the Γ-centered scheme, with 2 k-points per Å, leading to 2 x 2 x 3 mesh. Temperature effects were not included in the DFT calculations. Similar DFT-based approach has been demonstrated to reasonably well reproduce the phase transition boundaries in the $MgSiO_3$ pyroxene system in earlier studies (Yu and Wentzcovitch 2009).

Results and Discussion

Single-crystal X-ray diffraction experiments performed between 9.5 and 50 GPa revealed two clinoenstatite phases. The first phase, observed at six pressure points spanning 9.5-35.5 GPa, was successfully indexed using the monoclinic *C*2/*c* space group. Crystal reflections remained sharp, in this pressure range, suggesting a lack of deviatoric stresses. Variation of the unit-cell parameters with pressure (Table 2) shows a continuously decreasing trend up to 35.5 GPa. Refined lattice parameters agree well with the previously reported high-pressure clinoenstatite *C*2/*c* phase (Angel and Hugh-Jones 1994; Shinmei et al. 1999). At 45 GPa clinoenstatite underwent a sudden volume decrease indicating that a first-order phase change occurred between 41.34 and 45 GPa. Quality of data collected around this pressure range is too low for quantitative analysis. The next viable data was collected at 50.2 GPa. Data quality from this single pressure point is too low for single-crystal structure refinement, however the measured lattice parameters and accompanying DFT calculations indicate the transition from HPCEN to HPCEN2 as in diopside (Plonka et al. 2012; Hu et al. 2016) and clinoferrosilite (Pakhomova et al. 2017). Structural evolution of clinoenstatite with pressure is shown in Figure 1.

The lattice parameters and volume of HPCEN as a function of pressure (Table 2) were fitted with a third-order Birch-Murnaghan equation of state. The HPCEN-*C*2/*c* reference volume

This is a preprint, the final version is subject to change, of the American Mineralogist (MSA)
Cite as Authors (Year) Title. American Mineralogist, in press.
DOI: https://doi.org/10.2138/am-2019-6740

(V_o) was refined during the least-squares fitting procedure because HPCEN-*C*2/*c* is unquenchable (Angel et al. 1992; Ross and Reynard 1999). Fitting was performed using the Burnman Python library (Cottaar et al. 2014). Our refined V_0 of 406(1) Å^3 agrees well with previously reported values of 405(2) Å^3 (Shinmei et al. 1999), 406(1) Å^3 (Angel and Hugh-Jones 1994), and 403.95 Å^3 (Jacobsen et al. 2010).

In order to fit the equation of state with a 0 GPa reference pressure, extrapolation from 9.5 GPa to room pressure leads to large experimental uncertainties in equation of state parameters. To improve statistics, we fitted a merged data set consisting of our 9.5-35.5 GPa compression data and the dataset from Angel and Hugh-Jones (1994). A third-order Birch-Murnaghan equation of state fitted to the merged data set gives the parameters: V_0 = 406(1) Å^3, K_{T0} = 103(8) GPa, and K_0' = 5.4(6).

We also performed EoS fitting following the procedure outlined in Jacobsen et al. 2010, to calculate the theoretical zero-pressure reference equation of state parameters, for the HPCEN phase. This method minimizes uncertainties in V_0, K_{T0}, and K_0' by using the lowest pressure data as a reference point and then extrapolating to "negative pressure" to obtain theoretical zero-pressure EoS parameters. Using 5.34 GPa as our reference pressure, and assuming a third-order Birch-Murnaghan EoS, we obtain $V_{5.34}$ = 388.1(2) Å^3, $K_{5.34}$ = 130(5) GPa, and $K_{5.34}$' = 5.1(5). After extrapolation, we obtain theoretical zero-pressure parameters: V_0 = 406.44 Å^3, K_{T0} = 102.2 GPa, and K_0' = 5.48. The Angel and Hugh-Jones (1994) dataset offers high data density near the reference pressure while data from this study provides a large pressure range. Therefore, we anticipated an improvement in uncertainties and a potential difference between the original fitted parameters and the theoretical zero-pressure parameters. However, the theoretical values are

This is a preprint, the final version is subject to change, of the American Mineralogist (MSA)
Cite as Authors (Year) Title. American Mineralogist, in press.
DOI: https://doi.org/10.2138/am-2019-6740

nearly identical to our fitted zero-pressure parameters, indicating the validity and precision of the fitted parameters.

Using the merged data set, the fitted HPCEN-*C*2/*c* phase equation of state and volume compression data are illustrated in Figure 2. We plotted our P-V data as normalized stress, $F_E = P/3f_E(1+2f_E)^{5/2}$, vs. Eulerian finite strain, $f_E = [(V_o/V)^{2/3} - 1]/2$ in Figure 3 with $V_0 = 406(1)$ Å^3. From the intercept and slope of a linear fit (a third-order Birth-Murnaghan equation of state) to the F_E- f_E plot, we obtain $K_{T0} = 103(1)$ GPa and $K_0' = 4.7(1)$. The positive slope and linear fit of the F_E- f_E plot reinforces the conclusion that our data are well described by a third-order Birch-Murnaghan EoS.

A comparison of equation of state parameters for HPCEN-*C*2/*c* with published data is given in Table 3. To a 3σ (99.7%) confidence level, published parameters agree with results presented here. While reported values fall primarily within the estimated standard deviations of our results, when taking the covariance from the fit of our P-V data into account we notice the reported K_0' from Angel and Hugh-Jones (1994) is inconsistent with our P-V data, Figure 4. This can be attributed to their fixing of K_0' to 6.6, the K_0' value obtained for their LPCEN, during equation of state refinement. When Angel and Hugh-Jones (1994) HPCEN data is re-fit with a fixed K_0' of 5.4 the K_{T0} grows to 111(6) GPa. The large misfit is likely due to the limited data range of Angel and Hugh-Jones (1994).

The variation in linear dimension, *l*, of a material can be expressed as linear compressibility, defined as $\beta_l = (-l)^{-1}(\delta l/\delta P)$. For linear parameters such as *a*, *b*, *c* we assess their compressibility by treating the cube of each parameter as volume in a Birch-Murnaghan EoS fitting procedure (Angel et al. 2014). The choice of EoS order was again made based on the F_E - f_E plot. A horizontal linear fit to the F_E - f_E plot for all unit-cell parameters prompted our selection

This is a preprint, the final version is subject to change, of the American Mineralogist (MSA)
Cite as Authors (Year) Title. American Mineralogist, in press.
DOI: https://doi.org/10.2138/am-2019-6740

of a second-order Birch-Murnaghan equation of state, K_0' = 4. For HPCEN-*C*2/*c*, our fitted linear moduli to *a*, *b*, *c*, and *a*sinβ are 99(3), 101(2), 158(7), and 115(4) GPa, respectively. Subsequent axial compressibility values are β_a = 10.1(3) x 10^{-3}, β_b = 9.9(2) x 10^{-3}, β_c = 6.3(3) x 10^{-3}, $\beta_{a\sin\beta}$ = 8.7(3) x 10^{-3} GPa^{-1}.

Volume and axial compression of our HPCEN-*C*2/*c*, as compared to pyroxene phases belonging to the hedenbergite-diopside-ferrosilite-enstatite, $CaFeSi_2O_6$-$MgCaSi_2O_6$-$Fe_2Si_2O_6$-$Mg_2Si_2O_6$, quadrilateral system (Morimoto et al. 1989) are plotted in Figure 5. The evolution of HPCEN-*C*2/*c* lattice parameters with pressure differs slightly from that of other familial pyroxenes. Clinopyroxenes tend to follow the characteristic axial compressibility scheme $\beta_b > \beta_c \approx \beta_a > \beta_{a\sin\beta}$ (Angel and Hugh-Jones 1994; Nestola et al. 2004; Pakhomova et al. 2017; Tribaudino et al. 2001; Hu et al. 2015) however, our results show HPCEN-*C*2/*c* follows the axial compressibility scheme $\beta_a \approx \beta_b > \beta_{a\sin\beta} > \beta_c$.

With an exception for a minor deflection in the stiffness of *a* beginning around 12 GPa, each axial direction maintains a steady compression trend relative to the other parameters. In our observed compression scheme, the decrease in volume between 9.5 and 35.5 GPa is due primarily to compression of the *a* and *b* axes, while the stiffer *a*sinβ and *c* parameters contract relatively little. The different anisotropy scheme of the HPCEN-*C*2/*c* phase with respect to other pyroxenes shows that the HPCEN-*C*2/*c* structure evolves differently with pressure than other pyroxenes.

Within the quadrilateral family, the *b* dimension is unique with the magnitudes remaining relatively clustered and showing similar compressibilities throughout the observed pressure range. This observation breaks down for the other lattice parameters *a*, *c*, and β. Other quadrilateral pyroxenes differ from HPCEN-*C*2/*c* where lattice parameter *a* is significantly

This is a preprint, the final version is subject to change, of the American Mineralogist (MSA)
Cite as Authors (Year) Title. American Mineralogist, in press.
DOI: https://doi.org/10.2138/am-2019-6740

shorter than other pyroxenes. Lattice parameters, among pyroxenes in the quadrilateral family, are also dispersed in magnitude for *c* and β. Compression behavior of HPCEN-*C*2/*c* does not agree particularly well with any member of the quadrilateral but agrees most well with *C*2/*c*-clinoferrosilite. Over the observed pressure range evolution of *C*2/*c*-clinoferrosilite lattice parameters *c* and β agree remarkably well with those of HPCEN-*C*2/*c*.

HPCEN-*C*2/*c* High Pressure Structure Behavior

Structure refinements obtained at six pressure points between 9.5 and 35.5 GPa show the crystal maintained a *C*2/*c* space group symmetry throughout the pressure range. The structure of the HPCEN-*C*2/*c* phase is composed of three distinct polyhedra: one $Si1O_4$ tetrahedron and two octahedra, $Mg1O_6$ and $Mg2O_6$. The Si1 site is bonded to four oxygen atoms: O1, O2, O3A, and O3B. The bridging O3 atoms connect the chains of Si tetrahedra running parallel to the *c* crystallographic axis. The extremely kinked and O-rotated Si tetrahedral chain is a distinguishing feature of the HPCEN-*C*2/*c* phase. The O3-O3-O3 bond angle, a measure of rotation of individual Si tetrahedra, displays a decreasing trend with increasing pressure as seen in Figure 6. As the *c* axis shortens with increasing pressure the Si tetrahedra rotate forcing the O3-O3-O3 angle to decrease, by 2% over the observed pressure range, as the chain becomes increasingly kinked. The Si tetrahedra are non-ideal, with Si1-O bond lengths ranging from 1.569(2) Å (Si1-O2) to 1.666(2) Å (Si1-O3B) at 9.5 GPa. Quadratic elongation and angular variation, measures of polyhedral ideality, are 1.0043 and 17.75°, respectively, at 9.5 GPa. The Mg1 atom, occupying the M1 site, sits at the center of the first of two MgO_6 octahedra. MgO_6 octahedra, forms 3 unique bonds with O: Mg1-O1A, Mg1-O1B, and Mg1-O2. At 9.5 GPa the Mg1-O1A, Mg1-01B, and Mg1-O2 bond lengths are 2.001(2) Å, 2.07(2) Å, and 1.989(2) Å, respectively. The M1 quadratic elongation and angular variation are 1.0059 and 19.18°. The M1 octahedra are

This is a preprint, the final version is subject to change, of the American Mineralogist (MSA)
Cite as Authors (Year) Title. American Mineralogist, in press.
DOI: https://doi.org/10.2138/am-2019-6740

edge-sharing along the O1B-O1B edge. Mg2 forms three unique bonds: Mg2-O1, Mg2-O2, and Mg2-O3. In the more distorted M2 octahedra the Mg2-O3 bond is the longest at 2.170(2) Å while Mg2-O1 is 2.068(2) Å and Mg2-O2 is 1.977(2) Å. The quadratic elongation and angular variation for the M2 site are 1.0097 and 25.82°.

The HPCEN-*C*2/*c* structure refinements show the SiO_4 tetrahedra remain relatively incompressible compared to the MgO_6 octahedra. Mg1 and Mg2 octahedra show a 13.8% and 15.9% volume reduction over the pressure range 9.5 to 35.5 GPa, respectively, while Si tetrahedra show only a 4.7% volume reduction. Octahedral and tetrahedral volumes as a function of pressure as well as polyhedral compressibility determined by a second-order Birch-Murnaghan equation of state are shown in Figure 7. The HPCEN-2 polyhedra follow the β_{Mg2} = 14.3(1) x 10^{-3} > β_{M1} = 10.3(7) x 10^{-3} > β_{Si1} = 2.0(5) x 10^{-3} GPa^{-1} scheme, where beta represents the compressibility of the polyhedral units.

Within the relatively compressible Mg2 octahedron, the Mg1-O2 is the most compressible with $\beta_{Mg1\text{-}O2}$ = 11.7(7) x 10^{-3}, $\beta_{Mg1\text{-}O1A}$ = 5.9(8) x 10^{-3} GPa^{-1}, and the edge-sharing Mg1-O1B is the stiffest bond $\beta_{Mg1\text{-}O1B}$ = 5.7(9) x 10^{-3} GPa^{-1}. The deformed Mg2 bond compressibility values are: $\beta_{Mg2\text{-}O3}$ = 39.7(6) x 10^{-3}, $\beta_{Mg1\text{-}O2}$ = 11.7(8) x 10^{-3}, $\beta_{Mg1\text{-}O1}$ = 11(1) x 10^{-3} GPa^{-1}. The high compressibility of the M2 octahedra, specifically the soft Mg2-O3 bond, accommodates much of the volume reduction over the observed pressure range. The compressed Mg octahedra, relative to the Si1 tetrahedra, allow for the rotation of Si tetrahedra from S-rotated to O-rotated chains during the LPCEN to HPCEN phase transition, occurring between 6.5 and 7.1 GPa (Jacobsen et al. 2010; Angel et al. 1992). As pressure increases, the Mg octahedra continue to compress, further accommodating the overall volume reduction.

This is a preprint, the final version is subject to change, of the American Mineralogist (MSA)
Cite as Authors (Year) Title. American Mineralogist, in press.
DOI: https://doi.org/10.2138/am-2019-6740

The Si1 tetrahedra are far less compressible than the M octahedra, with a bulk modulus five times that of the M1 octahedra. The softest bond in the Si1 tetrahedra has a compressibility $\beta_{Si1\text{-}O1}$ = 3.4(4) x 10^{-3} GPa^{-1} and the least compressible bond is the Si1-O2 bond with a compressibility of $\beta_{Si1\text{-}O1}$ = 0.6(2) x 10^{-3} GPa^{-1}. Given the stiffness of the Si1 tetrahedra, the majority of the deformation in the tetrahedral chain is absorbed by the shrinking O3-O3-O3 bond angle. In addition to the non-polyhedral volume, overall compression of the HPCEN-*C*2/*c* unit-cell with pressure can then be summarized as being governed by the compression of Mg octahedra, primarily on the M2 site, and rotation of Si1 tetrahedra decreasing the O3-O3-O3 bond angle.

Unlike in the orthopyroxene system, we do not find a significant increase in stiffness with increasing Ca^{2+} substitution into the M2 octahedral site. Hugh-Jones and Angel (1997) observed an increase in K_{T0} of 14% with the substitution of very small amounts of Ca^{2+} into the M2 site. However, in comparison with the results of Tribaudino et al. (2000) who examined the high-pressure behavior of Ca-rich HPCEN up to 35.5 GPa, we only notice a difference of 2.7% in K_{T0} between the two end members. This promotes the validity of the use of pure end-member $MgSiO_3$ as a representative pyroxene in the Earth's upper mantle, within the diopside-enstatite solid solution.

HPCEN-*C*2/*c* to HPCEN2-*P*2_1/*c* phase transition

Above 35.5 GPa, HPCEN undergoes a first-order phase transition to a HPCEN-*P*2_1/*c* phase. Data quality from our single pressure point is too low to report a structure refinement. However, in strong agreement with our observations, our DFT calculations predict a phase transition to a *P*2_1/*c* phase at 35 GPa (Figure 8). Lattice parameters from our DFT calculations are compared to observations in Table 4.

This is a preprint, the final version is subject to change, of the American Mineralogist (MSA)
Cite as Authors (Year) Title. American Mineralogist, in press.
DOI: https://doi.org/10.2138/am-2019-6740

Three phases were considered in the DFT calculations: LPCEN, HPCEN and HPCEN2. Starting models for structure optimizations were taken from the crystallographic refinements performed in this study at 0 GPa for LPCEN, 10.4 GPa for HPCEN, and for HPCEN2 we adopted the $P2_1/c$ high pressure clinoferrosilite model reported by (Pakhomova et al. 2017). Structures of all three phases were fully optimized (all unit cell parameters and fractional atomic coordinates) at a set of fixed external pressures from 0 GPa to 50 GPa, with 5 GPa intervals. The GGA approximation is known to overestimate both the unit cell parameters, as well as the phase transition pressures; however, as reported in Table 4, we obtained a reasonably good agreement with experimental results.

Our calculations predict that at 0K the HPCEN structure becomes energetically favorable over the LPCEN structure at about 5 GPa, which is consistent with experimental observations. The transformation from HPCEN to HPCEN2 is predicted at approximately 35 GPa, which is slightly lower than the experimental observation (45 GPa), but reasonable for the GGA approximation.

Implications

Observation of the HPCEN2 phase in $Mg_2Si_2O_6$ completes the third apex of the pyroxene quadrilateral wherein HPCEN2 is found, facilitating a broader view of clinopyroxene crystal chemistry at conditions relevant to metastability in the Earth's mantle along cold subduction geotherms. In addition, the wide pressure stability of the C2/c phase may become significant when considering slab mineralogy and morphology. Similarly, the C2/c diopside end-member displays a continuous compression trend up to 45.6 GPa (Plonka et al. 2012; Tribaudino et al. 2000) prior to transforming to the high-pressure $P2_1/c$ structure. At 1650°C, nearly all

This is a preprint, the final version is subject to change, of the American Mineralogist (MSA)
Cite as Authors (Year) Title. American Mineralogist, in press.
DOI: https://doi.org/10.2138/am-2019-6740

clinopyroxenes transform to garnet by 20 GPa (Gasparik 1989). However, it has been shown that the pyroxene-garnet transformation can be significantly inhibited at low temperature (<1550°C) (Nishi et al. 2008). Pyroxenes subducted into the mantle by cold downwelling slabs could potentially be kept below temperatures of 1500°C down to depths of ~1000 km (Bina et al. 2001).

As all of our experiments were performed at room temperature, the most that we can say about the thermal effects is that previous work (Nishi et al. 2008, van Mierlo et al. 2013) has indicated that pyroxenes may persist metastably to ~1500°C, temperatures corresponding to depths well into the ambient mantle transition zone and even deeper for cold slabs. To this we can now add knowledge of the structure and elastic properties of metastable clinoenstatite (at 300 K) to at least 35 GPa, pressures well into the top of the lower mantle. The structures and elastic properties of metastable pyroxenes are necessary for the modeling of slab dynamics driven by density and therefore buoyancy forces. However, the temperature effects on metastable phases must first be determined. Therefore, further studies are required to constrain the transformation temperatures of HPCEN to HPCEN2 at high pressure as well as the implications of pyroxene metastability on slab dynamics in the mantle.

Acknowledgements

This research was supported through grants from US National Science Foundation EAR-1452344 to SDJ and EAR-1722969 to PD. Support was also provided by the Carnegie/DOE Alliance Center (CDAC). Development of the ATREX software used for data analysis was supported by NSF grant EAR1440005. Portions of this work were performed at HPCAT (Sector 16) of the Advanced Photon Source (APS), Argonne National Laboratory. HPCAT operations

325 are supported by DOE-NNSA under Award No. DE-NA0001974, with partial instrumentation
326 funding by NSF. The Advanced Photon Source is a U.S. Department of Energy (DOE) Office of
327 Science User Facility operated for the DOE Office of Science by Argonne National Laboratory
328 under Contract No. DE-AC02-06CH11357. We thank Sergey Tkachev for gas-loading diamond-
329 anvil cells in the GSECARS gas-loading system, which is supported by COMPRES, the
330 Consortium for Materials Properties Research in Earth Sciences under NSF Cooperative
331 Agreement EAR 1606856.
332

References

Agrusta, R., Van Hunen, J., Goes, S. (2014). The effect of metastable pyroxene on the slab dynamics. Geophysical Research Letters, 41(24), 8800–8808. http://doi.org/10.1002/2014GL062159

Akaogi, M., Akimoto, S. (1977). Pyroxene - garnet solid-solution equilibria in the systems $Mg_3Si_4O_{12}$-$Mg_3Al_2Si_3O_{12}$ and $Fe_4Si_4O_{12}$-$Fe_3Al_2Si_3O_{12}$ at high pressures and temperatures. Physics of the Earth and Planetary Interiors, 15, 90–106.

Akashi, A., Nishihara, Y., Takahashi, E., Nakajima, Y., Tange, Y., Funakoshi, K. (2009). Orthoenstatite/clinoenstatite phase transformation in $MgSiO_3$ at high-pressure and high-temperature determined by in situ X-ray diffraction: Implications for nature of the X discontinuity. Journal of Geophysical Research., 114, B04206.

Angel, R. J., Chopelas, A., Ross, N. L. (1992). Stability of high-density clinoenstatite at upper-mantle pressures. Nature, 355, 322–324.

Angel, R. J., Gonzalez-Platas, J., Alvaro, M. (2014). EosFit7c and a Fortran module (library) for equation of state calculations. Zeitschrift Fur Kristallographie, 229(5), 405–419.

Angel, R. J., Hugh-Jones, D. a. (1994). Equations of state and thermodynamic properties of enstatite pyroxenes. Journal of Geophysical Research, 99(B10), 19777–19783.

Bina, C. R. (2013). Mineralogy: Garnet goes hungry. Nature Geoscience, 6(5), 335–336. https://doi.org/10.1038/ngeo1804

Bina, C. R., Stein, S., Marton, F. C., Van Ark, E. M. (2001). Implications of slab mineralogy for subduction dynamics. Physics of the Earth and Planetary Interiors, 127(1–4), 51–66.

Cottaar, S., Heister, T., Rose, I., Unterborn, C. (2014). BurnMan: A lower mantle mineral physics toolkit. Geochemistry, Geophysics, Geosystems, 15(4), 1164–1179.

356 Dera, P., Zhuravlev, K., Prakapenka, V., Rivers, M. L., Finkelstein, G. J., Grubor-Urosevic,
357 O.,Tschaunder, O., Clark, S.M., Downs, R. T. (2013). High pressure single-crystal micro X-
358 ray diffraction analysis with GSE_ADA/RSV software. High Pressure Research, 33(3),
359 466–484.

360 Finkelstein, G. J., Dera, P. K., Duffy, T. S. (2015). Phase transitions in orthopyroxene (En90) to
361 49 GPa from single-crystal X-ray diffraction. Physics of the Earth and Planetary Interiors,
362 244, 78–86.

363 Gasparik, T. (1989). Transformation of enstatite - diopside - jadeite pyroxenes to garnet. Contrib
364 Mineral Petrol, 102, 389–405.

365 Hogrefe, A., Rubie, D. C., Sharp, T. G., Seifert, F. (1994). Metastability of enstatite in deep
366 subducting lithosphere. Nature. https://doi.org/10.1038/372351a0

367 Hu, Y., Dera, P., Zhuravlev, K. (2015). Single-crystal diffraction and Raman spectroscopy of
368 hedenbergite up to 33 GPa. Physics and Chemistry of Minerals, 42(7), 595–608.

369 Hu, Y., Kiefer, B., Bina, C. R., Zhang, D., Dera, P. K. (2017). High-Pressure γ-$CaMgSi_2O_6$:
370 Does Penta-Coordinated Silicon Exist in the Earth's Mantle? Geophysical Research Letters,
371 340–348.

372 Hugh-Jones, D. A., Angel, R. J. (1997). Effect of Ca^{2+} and Fe^{2+} on the equation of state of
373 $MgSiO_3$ orthopyroxene. Journal of Geophysical Research, 102, 12,333-12,340.

374 Irifune, T., Susaki, J., Yagi, T., Sawamoto, H. (1989). Phase transformations in diopside
375 $CaMgSi_2O_6$ at pressures up to 25 GPa. Geophysical Research Letters, 16(2), 187–190.

376 Jacobsen, S. D., Liu, Z., Boffa Ballaran, T., Littlefield, E. F., Ehm, L., Hemley, R. J. (2010).
377 Effect of H_2O on upper mantle phase transitions in $MgSiO_3$: Is the depth of the seismic X-

discontinuity an indicator of mantle water content? Physics of the Earth and Planetary Interiors, 183(1–2), 234–244.

King, S. D., Frost, D. J., Rubie, D. C. (2015). Why cold slabs stagnate in the transition zone. Geology, 43(3), 231–234. https://doi.org/10.1130/G36320.1

Kung, J., Li, B., Uchida, T., Wang, Y. (2005). In-situ elasticity measurement for the unquenchable high-pressure clinopyroxene phase: Implication for the upper mantle. Geophysical Research Letters, 32(1), 1–4.

Kung, J., Li, B., Uchida, T., Wang, Y., Neuville, D., Liebermann, R. C. (2004). In situ measurements of sound velocities and densities across the orthopyroxene high-pressure clinopyroxene transition in $MgSiO_3$ at high pressure. Physics of the Earth and Planetary Interiors, 147(1), 27–44.

Li, B., Neuville, D. R. (2010). Elasticity of diopside to 8 GPa and 1073 K and implications for the upper mantle. Physics of the Earth and Planetary Interiors, 183(3–4), 398–403.

Lin, C. (2004). Pressure-induced polymorphism in enstatite ($MgSiO_3$) at room temperature: clinoenstatite and orthoenstatite, 65, 913–921.

Mao, H. K., Xu, J., Bell, P. M. (1986). Calibration of the ruby pressure gauge to 800 kbar under quasi-hydrostatic conditions. Journal of Geophysical Research, 91(B5), 4673–4676.

Morimoto, N., Fabries, J., Ferguson, A. K., Ginzburg, I. V., Ross, M., Seifeit, F. A., Zussman, J. (1989). Nomenclature of pyroxenes. Canadian Mineralogist, 2(5), 198–221.

Nestola, F., Tribaudino, M., Boffa Ballaran, T. (2004). High pressure behavior, transformation and crystal structure of synthetic iron-free pigeonite. American Mineralogist, 89, 189–196.

Nishi, M., Kato, T., Kubo, T., Kikegawa, T. (2008). Survival of pyropic garnet in subducting plates. Physics of the Earth and Planetary Interiors, 170(3–4), 274–280.

Nishi, M., Kubo, T., Ohfuji, H., Kato, T., Nishihara, Y., Irifune, T. (2013). Slow Si-Al interdiffusion in garnet and stagnation of subducting slabs. Earth and Planetary Science Letters, 361, 44–49. https://doi.org/10.1016/j.epsl.2012.11.022

Pakhomova, A., Ismailova, L., Bykova, E., Bykov, M., Ballaran, T. B., Dubrovinsky, L. (2017). A new high-pressure phase transition in clinoferrosilite: In situ single-crystal X-ray diffraction study. American Mineralogist, 102(3), 666–673.

Plonka, A. M., Dera, P., Irmen, P., Rivers, M. L., Ehm, L., Parise, J. B. (2012). □-diopside, a new ultrahigh-pressure polymorph of CaMgSi2O6 with six-coordinated silicon. Geophysical Research Letters, 39, 2000–2003.

Qin, F., Wu, X., Zhang, D., Qin, S., Jacobsen, S. D. (2017). Thermal Equation of State of Natural Ti-Bearing Clinohumite. Journal of Geophysical Research: Solid Earth, 122(11), 8943–8951.

Rivers, M. L., Prakapenka, V. B., Kubo, A., Pullins, C., Hall, C. M., Jacobsen (2008). The COMPRES/GSECARS gas loading system for diamond anvil cells at the Advanced Photon Source. High Pressure Research, 28(3), 273–292.

Ross, N. L., Reynard, B. (1999). The effect of iron on the $P2_1/c$ to C2/c transition in $(Mg,Fe)SiO_3$ clinopyroxenes. European Journal of Mineralogy, 11(3), 585–589.

Sheldrick, G. M. (2008). A short history of SHELX. Acta Cryst, A64, 112–122.

Shinmei, T., Tomioka, N., Fujino, K., Kuroda, K., Irifune, T. (1999). In situ X-ray diffraction study of enstatite up to 12 GPa and 1473 K and equations of state. American Mineralogist, 84(10), 1588–1594.

Shiraki, K., Kuroda, N., Urano, H., Maruyama, S. (1980). Clinoenstatite in boninites from the Bonin Islands, Japan. Nature, 285, 31–32.

Tribaudino, M., Nestola, F., Meneghini, C., Bromiley, G. D. (2003). The high-temperature P2/C1-C2/c phase transition in Fe-free Ca-rich $P2_1/c$ clinopyroxenes. Physics and Chemistry of Minerals, 30(9), 527–535.

Tribaudino, M., Prencipe, M., Bruno, M., Levy, D. (2000). High-pressure behaviour of Ca-rich C2/c clinopyroxenes along the join diopside-enstatite ($CaMgSi_2O_6$-$Mg_2Si_2O_6$). Physics and Chemistry of Minerals, 27(9), 656–664.

Tribaudino, M., Prencipe, M., Nestola, F., Hanfland, M. (2001). A $P2_1/c$-C2/c high-pressure phase transition in $Ca_{0.5}Mg_{1.5}Si_2O_6$ clinopyroxene. American Mineralogist, 86(7–8), 807–813.

Ulmer, P., Stalder, R. (2001). The $Mg(Fe)SiO_3$ orthoenstatite-clinoenstatite transitions at high pressures and temperatures determined by Raman-spectroscopy on quenched samples. American Mineralogist, 86(10), 1267–1274.

Van Mierlo, W. L., Langenhorst, F., Frost, D. J., Rubie, D. C. (2013). Stagnation of subducting slabs in the transition zone due to slow diffusion in majoritic garnet. Nature Geoscience, 6(5), 400–403. https://doi.org/10.1038/ngeo1772

Zhang, L., Ahsbahs, H., Hafner, S. S., Kutoglu, A. (1997). Single-crystal compression and crystal structure of clinopyroxene up to 10 GPa. American Mineralogist, 82(3–4), 245–258.

450
451
452 **Table 1:** Structural refinement statistics for HPCEN.

P (Gpa)	9.5(1)	10.4(1)	17.0(2)	24.4(2)	30.1(3)	35.5(7)
Measured reflections	768	497	346	406	401	384
Unique reflections	442	218	153	159	160	155
Fo > 4sig(Fo)	441	218	151	159	121	153
Rint	7.90%	9.19%	14.97%	8.55%	8.975	7.90%
Rw for Fo > 4sig(Fo)	5.22%	5.89%	8.11%	7.01%	7.04%	6.01%
Rall	5.22%	5.89%	8.11%	7.01%	8.40%	6.09%
wR2	15.34%	15.71%	21.45%	16.44%	19.60%	16.52%
GooF	1.168	1.223	1.103	1.168	1.102	1.237
No. Parameters	21	21	21	21	21	21
Space group	*C*2/*c*	*C*2/*c*	*C*2/*c*	*C*2/*c*	*C*2/*c*	*C*2/*c*
Z	4	4	4	4	4	4
Absorption coefficient	0.152	0.079	0.159	0.164	0.169	0.172

453
454
455 **Table 2:** Lattice parameters of high-pressure clinoenstatite ($Mg_2Si_2O_6$, HPCEN) and HPCEN2 at
456 various pressures.

P (GPa)	Space Group	*a* (Å)	*b* (Å)	*c* (Å)	β (°)	V (Å^3)
9.5(1)	*C*2/*c*	9.163(2)	8.587(1)	4.875(1)	101.325(1)	376.2(2)
10.4(1)	*C*2/*c*	9.144(2)	8.5452(9)	4.8807(9)	101.25(2)	374.1(2)
17.0(2)	*C*2/*c*	8.965(3)	8.443(1)	4.847(1)	100.91(3)	360.3(2)
24.4(2)	*C*2/*c*	8.871(2)	8.3397(9)	4.7940(9)	100.46(2)	348.8(2)
30.1(3)	*C*2/*c*	8.804(2)	8.244(1)	4.749(1)	100.31(2)	339.2(2)
35.5(7)	*C*2/*c*	8.739(3)	8.190(1)	4.714(1)	100.22(2)	332.1(2)
50.2(9)	$P2_1/c$	8.688(2)	7.828(2)	4.5840(9)	100.46(2)	306.6(1)

457
458 **Table 3:** Equation of state parameters for high-pressure clinoenstatite (HPCEN).

P-range (GPa)	V_0 (Å^3)	K_{T0} (GPa)	K_0' (GPa)	ρ_0 (g/cm^3)	Reference
9.5 - 35.5	406(1)	103(8)	5.4(6)	3.28(1)	This study
7.1 - 8.06	404	118	6.1	3.302	Jacobsen et al. (2010)
4.0 - 10.7	405(2)	106(17)	5(3)	3.292(14)	Shinmei et al. (1999)

5.3 - 8.0	406(1)	104(6)	6.6*	3.288(9)	Angel and Hugh-Jones (1994)

*Fixed during refinement.

459 **Table 4:** Coefficients obtained from fitting a Birch-Murnaghan EoS.

	LPCEN - DFT	HPCEN	HPCEN- DFT	HPCEN2	HPCEN2 - DFT
	$P2_1/c$	$C2/c$	$C2/c$	$P2_1/c$	$P2_1/c$
a_0 (Å)	9.7271	9.4389	9.5082	-	9.4665
a_{50}	9.0531	8.5831	8.7533	8.688(2)	8.7605
b_0 (Å)	8.9233	8.8450	8.9345	-	8.4573
b_{50}	8.0766	8.0519	8.1040	7.828(1)	7.9189
c_0 (Å)	5.2224	4.9739	5.0535	-	4.9209
c_{50}	4.8182	4.6336	4.6982	4.5840(9)	4.6096
β_0 (°)	108.46	101.91	102.89	-	98.08
β_{50}	107.65	99.36	99.86	100.46(2)	100.18
V_0 (Å^3)	429.96	406(1)	418.47	-	390.06
V_{50}	335.71	316.92	328.36	306.6(1)	314.74
K_{T0} (GPa)	107(1)	103(8)	106(2)	-	138(1)
K_0' (GPa)	5.1(1)	5.3(7)	5.6(2)	-	4.89(9)
ρ_0 (g/cm^3)	3.102	3.28(1)	3.187	-	3.419
ρ_{50}	3.972	4.208	4.063	4.350	4.237

[a] Parameters from extrapolation of equation of state.
$_{50}$ determined at 50 GPa

460

461

462

463

464

465

466

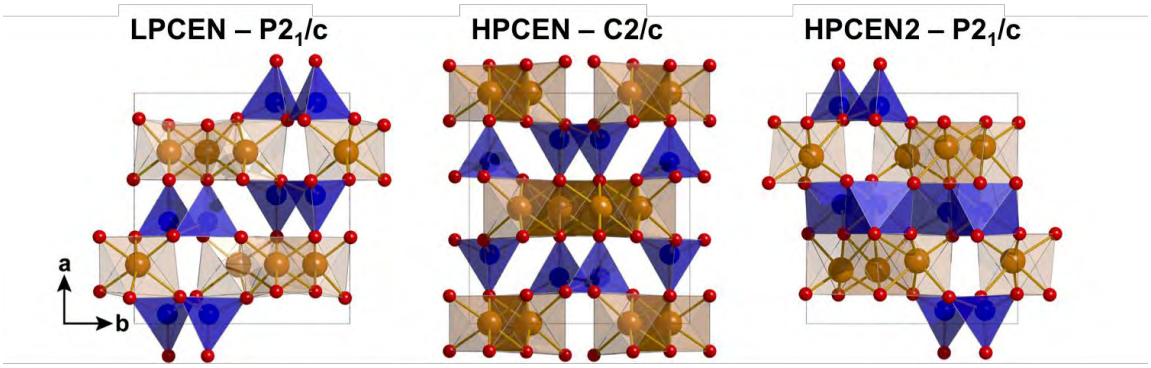

Figure 1: The three monoclinic structures of $Mg_2Si_2O_6$ (clinoenstatite): Left, low-pressure clinoenstatite (LPCEN) stable up to ~6 GPa. Middle, the unquenchable high-pressure clinoenstatite (HPCEN) stable at 6-45 GPa. Right, high-pressure clinoenstatite-2 (HPCEN2), observed at ~45 GPa in the current study. HPCEN2 structure shown here has been calculated using DFT. The edge-sharing Mg octrahedra are shown in yellow and corner-sharing silica tetrahedra are shown in blue. The HPCEN2 phase features edge-sharing octahedral Si, also shaded blue.

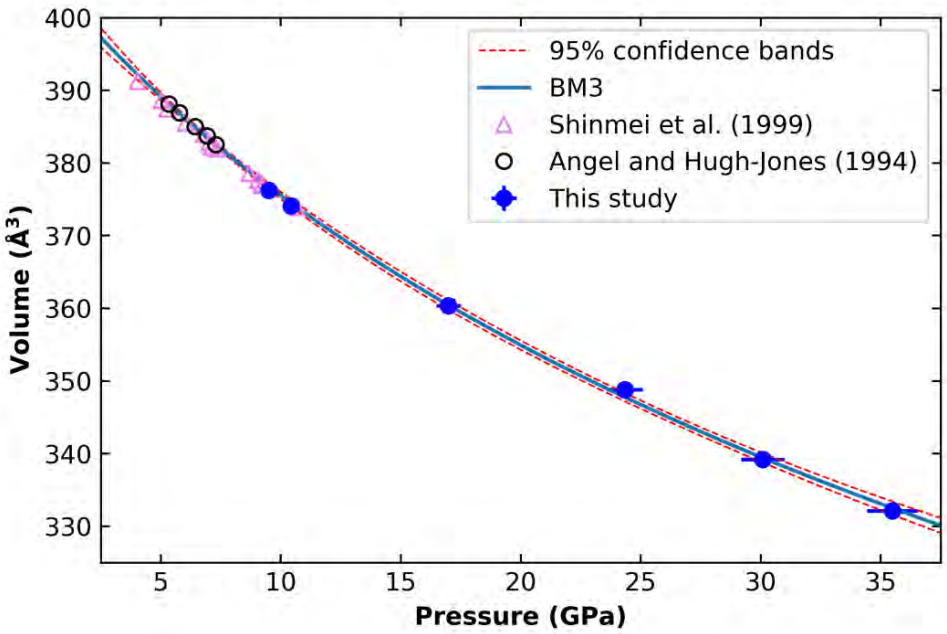

Figure 2: Comparison of variation in unit-cell volume as a function of pressure in anhydrous $MgSiO_3$ high-pressure clinoenstatite. Third-order Birch-Murnaghan equation of state for the solid blue curve is given in Table 3.

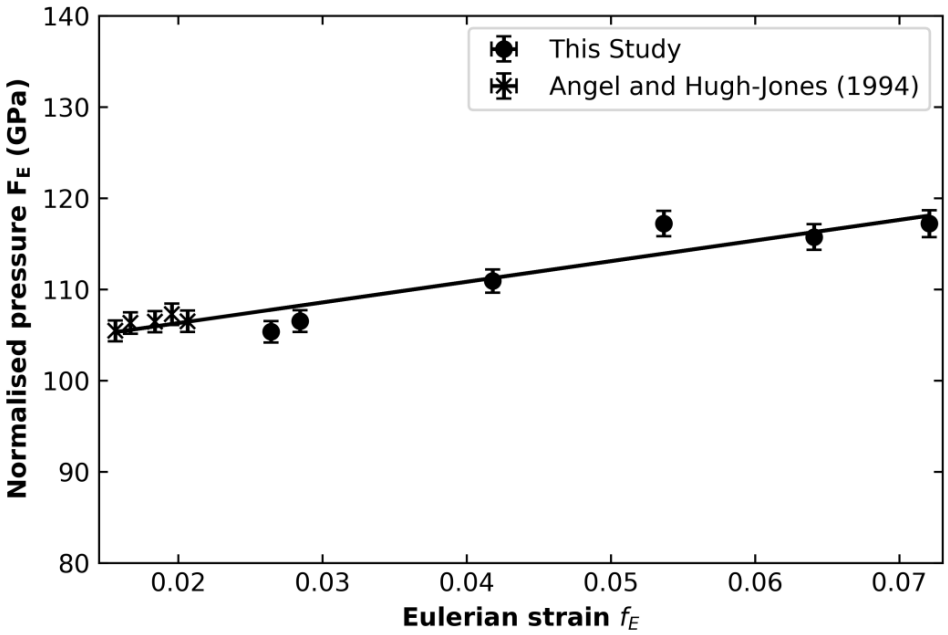

494

495 **Figure 3:** Normalized stress F_E vs. the Eulerian strain f_E for HPCEN.

496

497

498

499

500

501

502

503

This is a preprint, the final version is subject to change, of the American Mineralogist (MSA)
Cite as Authors (Year) Title. American Mineralogist, in press.
DOI: https://doi.org/10.2138/am-2019-6740

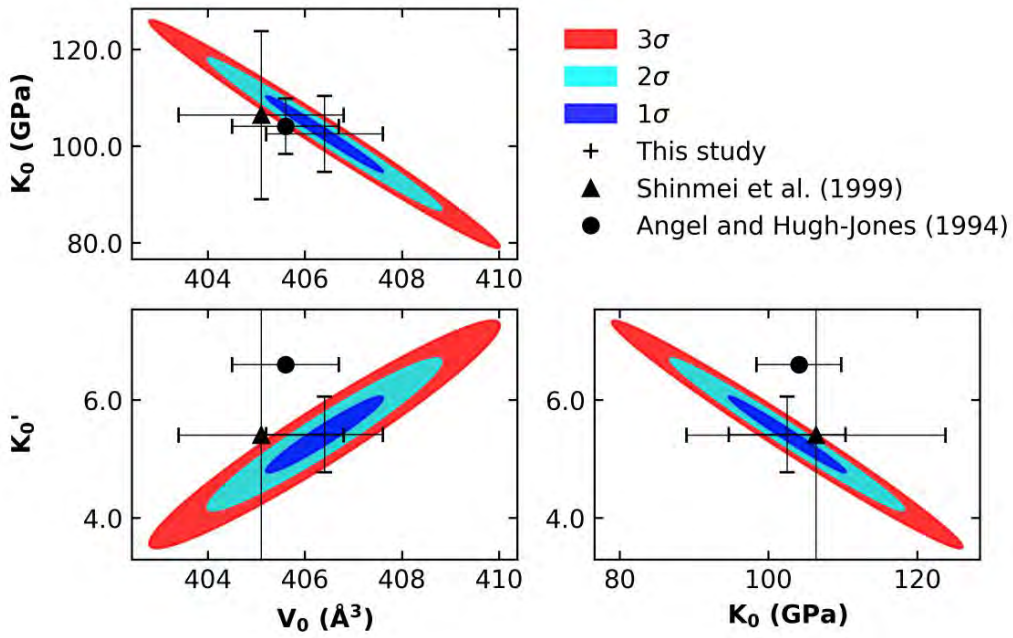

504

505 **Figure 4:** Confidence ellipse of isothermal equation of state parameters for third-order Birch-
506 Murnaghan equation of state. Note that the limits of the error bars correspond to 1 estimated
507 standard deviation (*esd*). Previously reported results match well with those reported here, except
508 for the reported K_0' from Angel and Hugh-Jones (1994). This is most likely a consequence of
509 their fixing K_0' to 6.6 during the fitting procedure.

510

This is a preprint, the final version is subject to change, of the American Mineralogist (MSA)
Cite as Authors (Year) Title. American Mineralogist, in press.
DOI: https://doi.org/10.2138/am-2019-6740

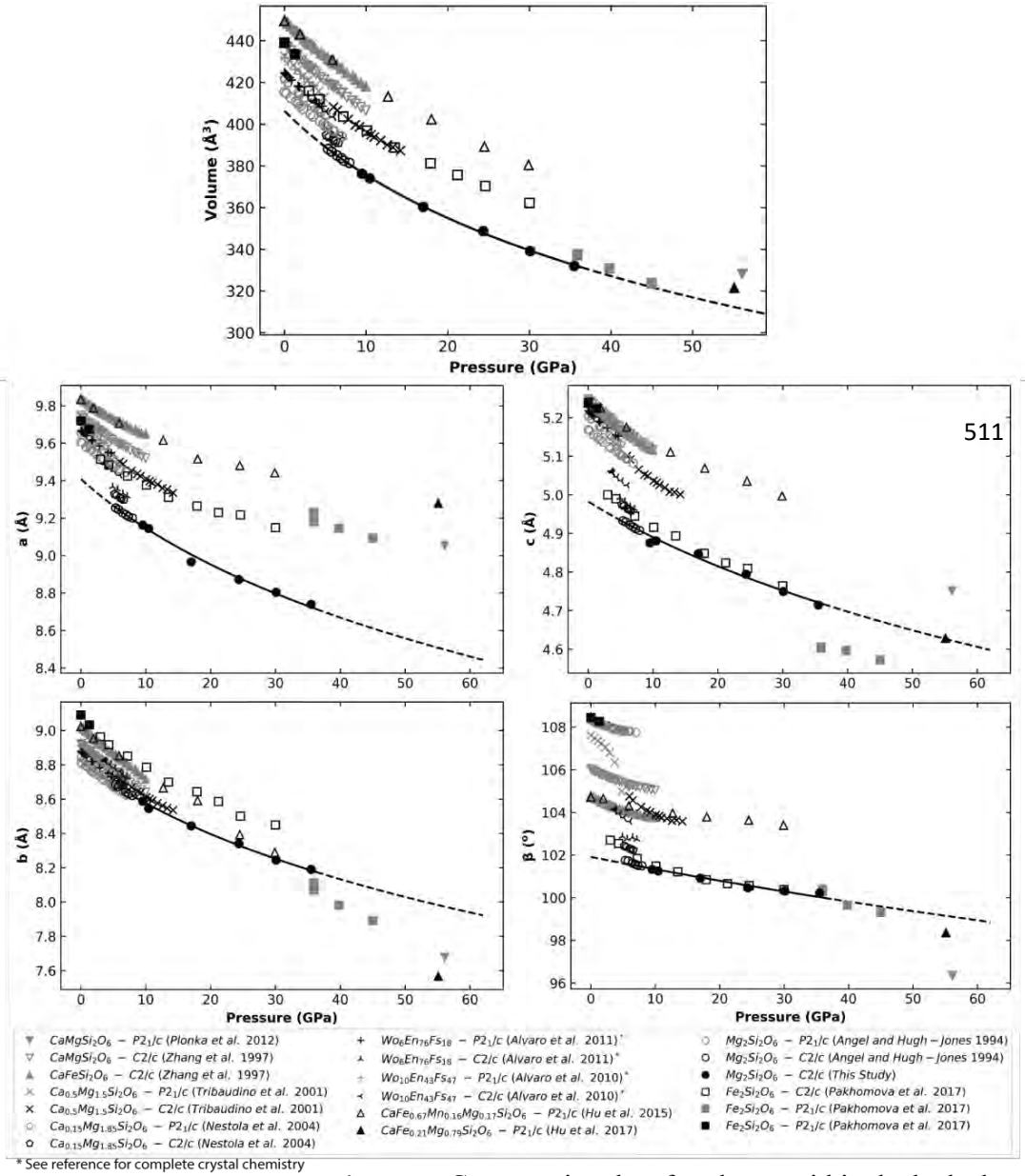

Figure 5: Compression data for phases within the hedenbergite-diopside-ferrosilite-enstatite quadrilateral. Solid line represents the Birch-Murnaghan EoS fits to the current experimental data for HPCEN, extrapolated beyond the data points with dashes.

This is a preprint, the final version is subject to change, of the American Mineralogist (MSA)
Cite as Authors (Year) Title. American Mineralogist, in press.
DOI: https://doi.org/10.2138/am-2019-6740

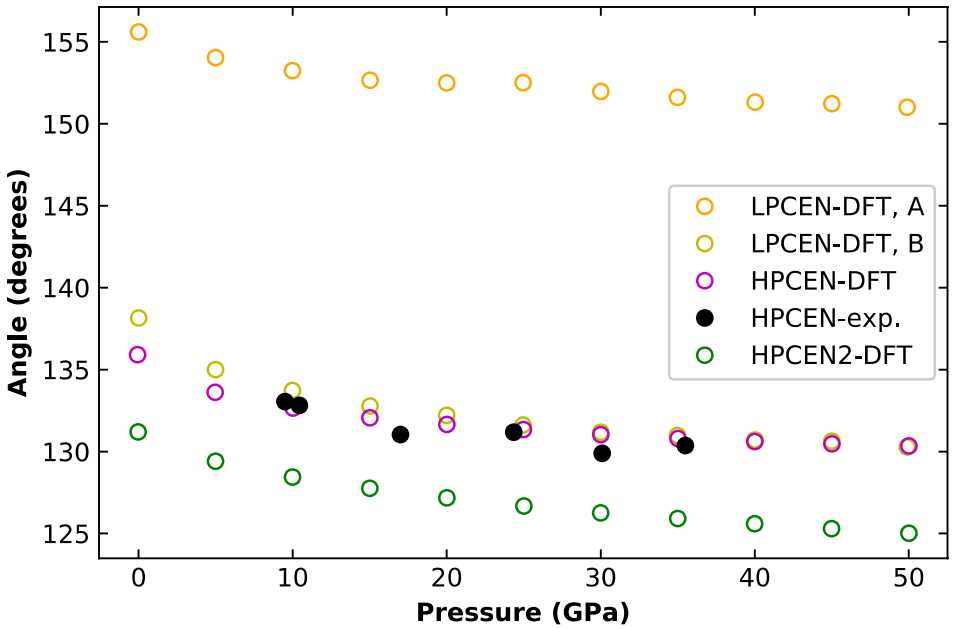

Figure 6: O3-O3-O3 angle (solid dots), a measure of rotation of Si tetrahedral units along the pyroxene chains. The kinking angle reduces by 2% over the experimental pressure range as the (001) axis shortens.

This is a preprint, the final version is subject to change, of the American Mineralogist (MSA)
Cite as Authors (Year) Title. American Mineralogist, in press.
DOI: https://doi.org/10.2138/am-2019-6740

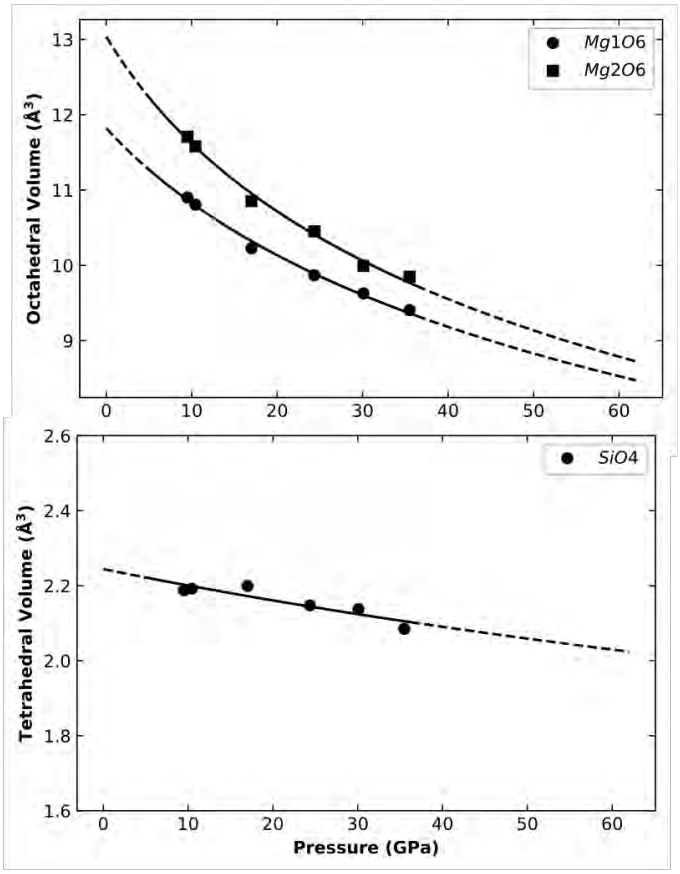

527

528 **Figure 7:** Pressure-volume trends of octahedral (Mg) and tetrahedral (Si) sites in HPCEN in

529 *C*2/*c*. Solid lines represent the second-order Birch-Murnaghan EoS fits.

530

531

532

533

534

535

This is a preprint, the final version is subject to change, of the American Mineralogist (MSA)
Cite as Authors (Year) Title. American Mineralogist, in press.
DOI: https://doi.org/10.2138/am-2019-6740

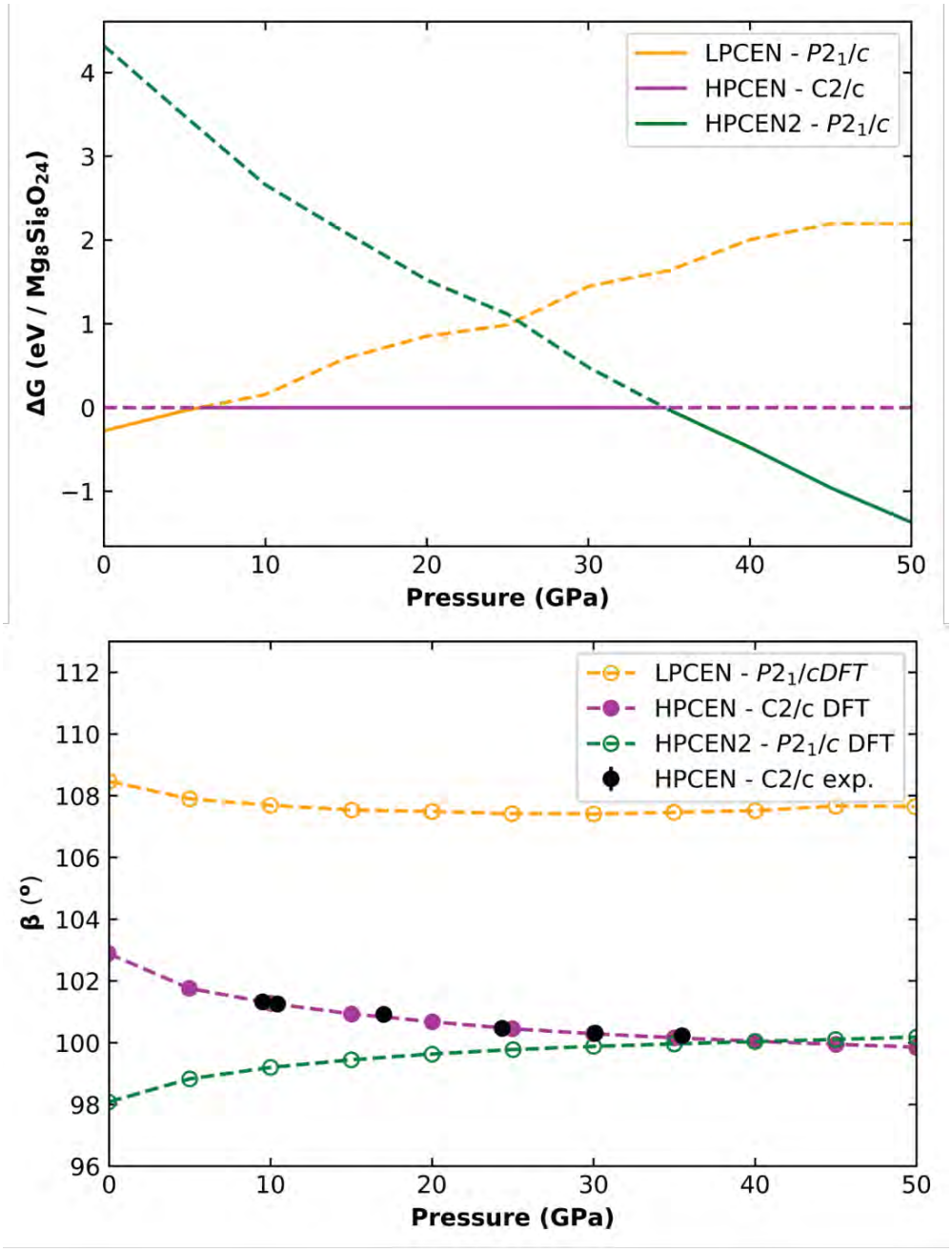

536

537 **Figure 8:** Density functional theory (DFT) results for the $Mg_8Si_8O_{24}$ system. (top) Change in
538 Gibbs free energy was calculated to determine phase transition pressures for clinoenstatite
539 showing a calculated phase transition from HPCEN to HPCEN2 at approximately 35 GPa.
540 (bottom) Experimental measurements agree well with calculated structure parameters.